NANO LETTERS

Letter

pubs.acs.org/NanoLett

Nanoscale Buckling of Ultrathin Low-*k* Dielectric Lines during Hard-Mask Patterning

Gheorghe Stan,*[†,‡] Cristian V. Ciobanu,*[§] Igor Levin,[†] Hui J. Yoo,[∥] Alan Myers,[∥] Kanwal Singh,[∥] Christopher Jezewski,[∥] Barbara Miner,[⊥] and Sean W. King[⊥]

[†]Material Measurement Laboratory, National Institute of Standards and Technology, Gaithersburg, Maryland 20899, United States

[‡]Department of Mechanical Engineering, University of Maryland, College Park, Maryland 20742, United States

[§]Department of Mechanical Engineering, Colorado School of Mines, Golden, Colorado 80401, United States

[∥]Components Research, Intel Corporation, Hillsboro, Oregon 97124, United States

[⊥]Logic Technology Development, Intel Corporation, Hillsboro, Oregon 97124, United States

Supporting Information

ABSTRACT: Commonly known in macroscale mechanics, buckling phenomena are now also encountered in the nanoscale world as revealed in today's cutting-edge fabrication of microelectronics. The description of nanoscale buckling requires precise dimensional and elastic moduli measurements, as well as a thorough understanding of the relationships between stresses in the system and the ensuing morphologies. Here, we analyze quantitatively the buckling mechanics of organosilicate fins that are capped with hard masks in the process of lithographic formation of deep interconnects. We propose an analytical model that quantitatively describes the morphologies of the buckled fins generated by residual stresses in the hard mask. Using measurements of mechanical properties and geometric characteristics, we have verified the predictions of the analytical model for structures with various degrees of buckling, thus putting forth a framework for guiding the design of future nanoscale interconnect architectures.

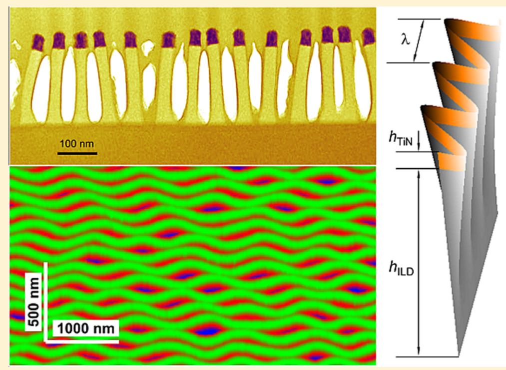

KEYWORDS: *low-k dielectric patterns, nanoscale buckling, interconnect circuits*

Technological advances in developing new fabrication methods, complex materials, and characterization tools are needed in the quest for scaling down integrated components[1,2] such as transistors and interconnects in high-performance electronics.[3,4] To this end, fabrication efforts have to address not only requirements for desired electronic functionalities but also challenging demands[5] on the mechanical integrity and robustness of nanoscale architectures. The characterization techniques that target mechanical properties have recently made significant advances toward accurate interrogation of the mechanical response of separated and integrated nanoscale building blocks[6−10] and is poised now to guide advanced designs for nanoscale circuitry. Testing and characterization of materials and structures integrated at the nanoscale are necessary because of the presence of size effects[7,11−13] and of the degradation of mechanical properties during multiple fabrication steps.[14,15] Because both size effects and degradation of properties are unavoidable in the next generations of densely integrated circuits, a fundamental understanding of the structure−property relationship, coupled with accurate characterization, is required in order to significantly improve the design, performance, and reliability of nanoscale devices.

Currently, in the dual damascene patterning of interlayer dielectric (ILD) structures for interconnects,[16,17] hard masks (e.g., TiN) are used to define ILD trenches with widths below one hundred nanometers.[18] The hard masks provide precise alignment and great chemical selectivity in defining nanoscale patterns on the ILD. However, because the ILD and the deposited TiN have very different structural and mechanical properties, there is a residual stress accumulated in the TiN hard mask which can generate high compressive stresses in the patterned structures. This becomes a drawback when the ILD lines are thinner and taller because mechanical instabilities can occur in ILD lines that are fabricated below certain dimensions, for example, thinner than 50 nm and taller than 100 nm. These mechanical instabilities are in the form of wiggled lines, reminiscent of the classical buckling phenomenon. Similar instabilities[19−21] have been investigated for micron-scale structures either as potential components in stretchable electronic devices[6] or as phenomena underlying new metrologies.[22] Micron-scale buckling phenomena have been observed in thin films and strips,[23,24] whereas the nanoscale

Received: February 18, 2015
Revised: April 27, 2015
Published: May 7, 2015

DOI: 10.1021/acs.nanolett.5b00685
Nano Lett. 2015, 15, 3845−3850

patterned structures in this work are thin and tall lines (fins). Although observations of buckling in TiN-capped ILD fins have been reported,[25,26] detailed dimensional and mechanical measurements have not yet been performed for self-consistent diagnostics based on analytical or finite element modeling.

Here, we report results from accurate dimensional and mechanical characterization experiments and propose an analytical model for the buckling of TiN-capped ILD fins. We have performed dimensional measurements using atomic force microscopy (AFM), with the AFM tip scanning directly atop the buckled fins so as to measure the amplitude and wavelength of their undulations. In addition, we have measured the geometrical dimensions (width and height) of the patterned lines using AFM and transmission electron microscopy (TEM) on selected samples; we have also determined the elastic modulus of the patterned structures from contact-resonance AFM (CR-AFM) and the residual stress of the TiN films from measurements of wafer curvature. We have used the results of all these measurements in the buckling analysis model in order to achieve a consistent fundamental understanding of the observed buckling and to provide quantitative guidance for the mechanical response of the TiN-capped ILD fins fabricated at tighter pitches and higher aspect ratios.

Figure 1 shows the TiN-capped ILD fins investigated here, with a schematic of the TiN/ILD/SiO_2/Si stack structure displayed in Figure 1a and an AFM micrograph showing the topography of the buckled fins [Figure 1b] in the vicinity of a region where fins have been scraped down to the substrate. The samples investigated (labeled A through D) have been prepared on 300 mm-diameter Si(100) wafers, as described in the Methods section. The fins have been defined first by patterning the TiN film deposited on an ILD layer (areas of about 1 mm × 1 mm), and then exposing the ILD to plasma etch. As the etch of the ILD progresses through the slots patterned into the TiN film, the residual stress developed in the TiN layer during fabrication forces the entire fin (TiN cap and ILD ridge) into a buckling state. The etching depth is one of the main control parameters for buckling; at the same width, buckling is more pronounced for the fins that are patterned deeper [Figure 1c,d]. Using partially scraped samples, we have assessed the height of the fins from the height difference between the tops of original fins and the roots of the scraped fins [Figure 1b]. These height measurements are in excellent agreement with the dimensions obtained from TEM images [Figure 1c,d], which provide the widths and heights of the ILD fins and TiN caps. The dimensions are listed in Table 1, along with the elastic moduli of the caps and fins.

The elastic moduli of the TiN caps have been determined from nanoscale contact stiffness measurements. We have performed contact-resonance AFM (CR-AFM) measurements[7−9] on 300 nm wide strips of TiN films adjacent to the buckled lines [refer to Figure S1 in Supporting Information]. The wide TiN strips have been fabricated in the same way as the buckled lines, but, unlike the buckled lines, they provide a flat and straight support for the spherical AFM tip used during CR-AFM measurements (refer to Supporting Information for details on the determination of elastic moduli). The elastic moduli determined from CR-AFM are summarized in Table 1. All the measurement uncertainties reported in this paper represent one standard deviation from the mean of the measured values.

To quantitatively describe the morphology of the buckled fins, we have measured the lateral deflections of the TiN tops of the fins using AFM. For each sample, we have acquired three AFM micrographs of 7.5 μm × 7.5 μm (640 pixels ×640 pixels) at different locations within the patterned areas. The left column of Figure 2 shows selected regions of the AFM micrographs for samples A−D, with different amplitudes and wavelengths for each sample. We have traced the undulations of each buckled fin at the midpoint of its width. Examples of such traces are shown in the middle column of Figure 2. For each sample, we have assembled the traces acquired via AFM measurements into a large train of data and then performed Fourier analysis to determine the mean wavelength and standard deviation (refer to Supporting Information).

In the buckling analysis, each half-wavelength segment of an ILD ridge has been modeled as a thin plate simply supported along the x = 0 and x = $\lambda/2$ edges, built-in at the bottom edge

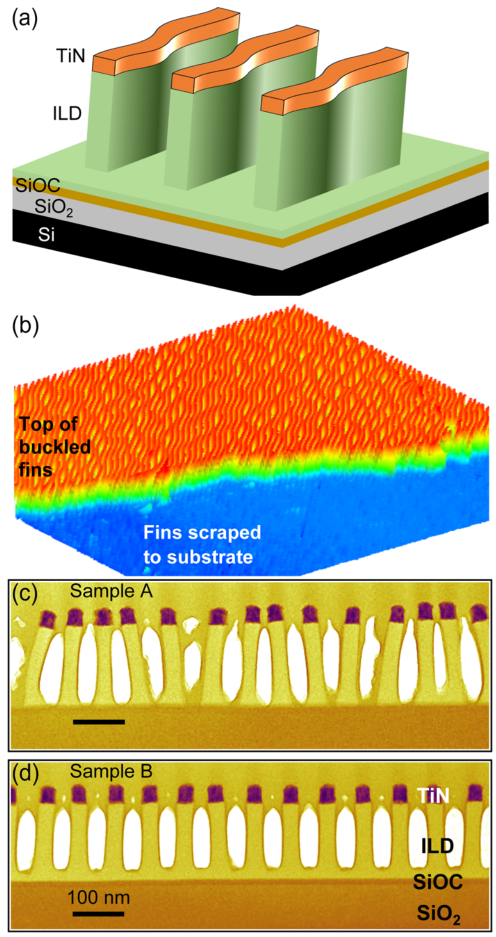

Figure 1. (a) Schematic of the stack structure of the TiN-capped ILD fins investigated in this work. (b) AFM micrograph showing the three-dimensional view of the tops and sides of the buckled fins. (c), (d) False-color cross-sectional TEM images of samples A and B, respectively, showing more pronounced buckling for the taller fins of sample A.

Table 1. Dimensions and Young's Moduli of the TiN Caps and ILD Ridges, for an Average Fin Width of 32 nm

sample	h_{ILD} (nm)	h_{TiN} (nm)	E_{ILD} (GPa)	E_{TiN} (GPa)
A	180	35	2.5 ± 0.3	185.8 ± 14.2
B	150	36	2.5 ± 0.3	185.8 ± 14.2
C	180	16	5.7 ± 1.1	210.0 ± 17.0
D	160	17	5.7 ± 1.1	210.0 ± 17.0

DOI: 10.1021/acs.nanolett.5b00685
Nano Lett. 2015, 15, 3845−3850

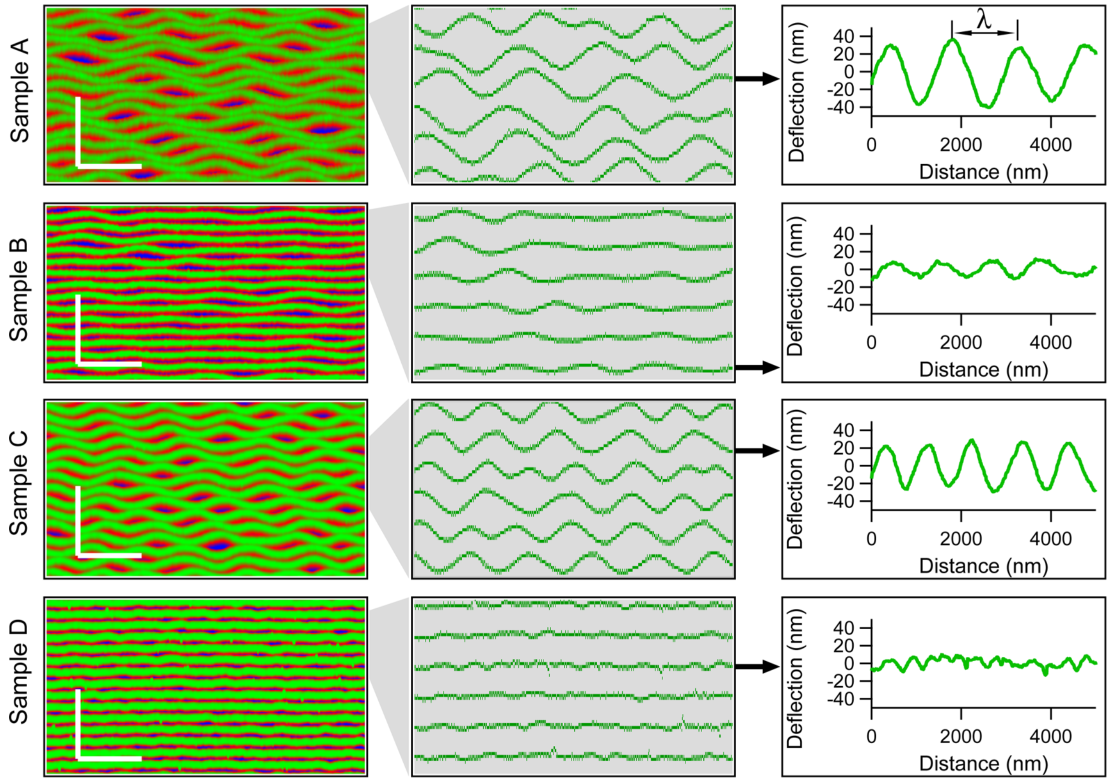

Figure 2. AFM analysis of the bucked lines for 1.250 μm × 5.000 μm regions of samples A–D. Left column: AFM micrographs of the tops of the buckled lines (horizontal and vertical scale bars are 1000 and 500 nm, respectively). Middle column: (b) Enlarged areas with traces of the buckled fins extracted from the AFM micrographs in the left column. Right column: Selected individual traces from each sample. The buckling wavelengths have been determined from Fourier analysis of the traces (buckled lines).

(y = 0), and connected with a TiN beam at the top edge, $y = h_{ILD}$ (refer to Figure 3). In Figure 3, h_{TiN} and h_{ILD} are the heights of the TiN cap and ILD plate, respectively, and the beam and plate have the same width d and length $\lambda/2$. The simply supported boundary conditions require zero bending moments at the inflection points x = 0 and $x = \lambda/2$, which ensures that these boundary conditions are appropriately used

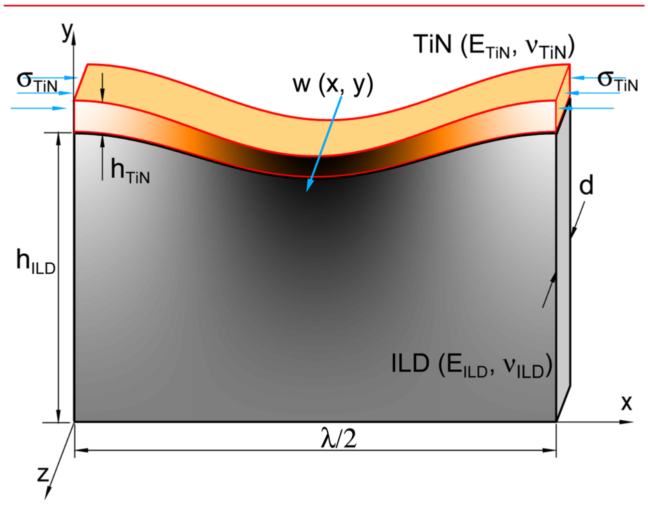

Figure 3. Out-of-plane deflection w of a buckled TiN-capped ILD fin over half-wavelength $\lambda/2$. Under the residual compressive stress σ_{TiN}, the buckling of the TiN beam is limited by the deformation of the ILD plate. E_{TiN} and E_{ILD} refer here to Young's moduli, and ν_{TiN} and ν_{ILD} to Poisson's ratios of beam and plate, respectively.

for describing the periodic form of the buckling wave, which has inflection points at $x = n\lambda/2$ along the beam, with n being any integer. The residual compressive stress σ_{TiN} in the TiN beam induces the buckling of the entire structure (beam and plate), with the work done by the compressive forces converted into bending energies of the beam and the plate. We have derived the critical buckling state of a TiN-capped ILD fin by adapting the solution proposed by Miles[27,28] for a rectangular plate with two edges simply supported, one edge built-in, and one edge supported by an elastic beam. Unlike Miles' solution, where the load is distributed uniformly along the simply supported edges, the (only) load in our case is provided by the compressive stress in the TiN beam. The reason for neglecting the stress in the ILD ridges is that this stress is 1 to 2 orders of magnitude smaller than the stress in the TiN beams. From wafer curvature measurements, the stress in the ILD films before patterning has been estimated at about 65 MPa, which is well below the minimum critical buckling stress[28] (about 200 MPa) of the ILD ridges investigated in this work. Indeed, due to their small residual stress, the ILD ridges recover from their buckling upon removal of the TiN caps. Furthermore, due to the large difference in stiffness between the stiff TiN beam and the compliant ILD ridge, the ridge-beam interface is described as a plate supported by an elastic beam because the twisting moments transmitted from the complaint ILD ridge to the stiff TiN beam are negligible.[28] Under these assumptions, we have explicitly calculated (details provided in Supporting Information) the critical stress σ_{TiN} that causes buckling as a function of the wavelength λ of the mth order buckling state (m = 1 for the first order, m = 2 for the second order, etc.)

DOI: 10.1021/acs.nanolett.5b00685
Nano Lett. 2015, 15, 3845–3850

$$\sigma_{\mathrm{TiN}} = \frac{\kappa^2 E_{\mathrm{TiN}} I_{\mathrm{TiN}}}{4h_{\mathrm{ILD}}^2 A_{\mathrm{TiN}}} + \frac{\kappa D_{\mathrm{ILD}}}{4h_{\mathrm{ILD}} A_{\mathrm{TiN}}(-\kappa + \sinh\kappa)} \left[4 + (1+\nu_{\mathrm{ILD}})^2 + \frac{\kappa^2(1-\nu_{\mathrm{ILD}})^2}{2} - (\nu_{\mathrm{ILD}} - 1)(\nu_{\mathrm{ILD}} + 3)\cosh\kappa\right] \tag{1}$$

where $D_{\mathrm{ILD}} = (1/12)E_{\mathrm{ILD}}d^3/(1-\nu_{\mathrm{ILD}}^2)$ is the flexural rigidity of the plate, $\kappa = 4m\pi h_{\mathrm{ILD}}/\lambda$, and $A_{\mathrm{TiN}} = h_{\mathrm{ILD}}d$ and $I_{\mathrm{TiN}} = h_{\mathrm{TiN}}d^3/12$ are the area and the moment of inertia of the cross section of the TiN beam, respectively. We note that relations between the critical stress and the buckling wavelength can in general be obtained from minimizing energy using variational trial solutions.[24,29] Energy minimization approaches are most effective in cases where a rigorous solution of the deflection equation cannot be readily derived, and therefore variational approximations would be sufficient; here, it was possible to derive the exact analytical solution, in the form of eq 1.

Equation 1 is the main result of our analysis and also constitutes an implicit relation from which the buckling wavelength is extracted in terms of the critical stress and the geometric and material parameters of the fins: as such, eq 1 provides a framework for comparisons with our wavelength measurements (see Figure 4). Experimentally, the wavelengths

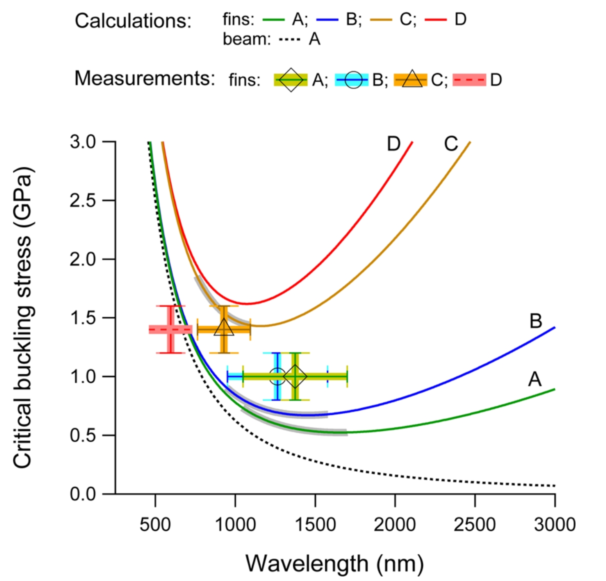

Figure 4. Measured critical buckling stresses and wavelengths (marks with error bars) compared to the results of buckling analysis (curves). The critical stress as a function of wavelength for a free TiN beam cap (unattached to any fin) is also shown for comparison (black dotted curve). The highlighted portions of the theoretical curves correspond to the observed experimental wavelength ranges for each sample.

of the buckled fins have been obtained from AFM scans as described above and in Figure 2, and the residual stresses have been determined from wafer curvature measurements before patterning. Being performed prior to patterning, the residual stress measurements provide only an indication of the average values of the stress of the TiN mask. It is also plausible that the residual stress in the patterned TiN film could further undergo local variations during processing. Therefore, the error bars for the stress measurements shown in Figure 4 are lower bounds on the uncertainty in stress, and they correspond to one standard deviation from the mean of the measurements. Nevertheless, the measurement results show good agreement with the theoretical curves of the buckling critical stress versus wavelength for all the investigated samples. The stress–wavelength dependencies are calculated for the first buckling modes, $m = 1$, of each sample with the parameters given in Table 1. For each pair of samples (A and B; C and D) the range of the induced wavelengths is different. Also, within each pair, the sample with shallower trenches (B for the first pair, and D for the second pair) exhibits shorter wavelengths and, theoretically, its minimum critical stress for buckling should be higher. This behavior resembles the out-of-plane buckling of compressively strained free-hanging films[30] and polymer ridges.[31,32]

The comparison shown in Figure 4 between the measured wavelengths (Figure S4 in Supporting Information) and the calculated stress–wavelength dependencies [eq 1] suggests that stresses from 0.5 to 0.9 GPa induce buckling in samples A and B with wavelengths in the 950 to 1700 nm range and that stresses from 1.4 to 1.8 GPa induce wavelengths in the 800 to 1200 nm range in sample C. The mean wavelengths in samples A, B, and C are observed for stresses that are above the minimum critical stresses at which buckling is induced in each sample. The induced buckling wavelengths are obtained when the work done by the residual stresses is balanced by the bending energies of the TiN beam caps and ILD ridges. This means that the buckling condition for a given observed wavelength is fulfilled by the existing residual stresses in the TiN beam caps, which are, in general, above the minimal critical stresses. The calculated stress values are comparable with those measured from wafer curvature prior to processing: 1.0 ± 0.2 GPa for samples A and B and 1.4 ± 0.2 GPa for samples C and D. Of interest for the design of buckle-free structures would be the minimal critical stress at which buckling appears first, which accordingly with Figure 4 is about 0.5 to 0.7 GPa for samples A and B and 1.4 to 1.6 GPa for samples C and D, respectively.

In contrast to samples A–C, the small-amplitude undulations observed in sample D do not have a well-defined, long-range spatial periodicity (refer to Supporting Information). In sample D, the buckling state occurs in the form of small-amplitude isolated bursts (Figure 2, also Figure S4b in Supporting Information), rather than undulations with nearly uniform wavelength along the fins. This observation of an incipient, burst-like buckling state for sample D indicates that the residual stress of the TiN film is smaller than the minimum critical stress required for inducing buckling with uniform wavelength (Figure 4). The discontinuous buckling state along the fins could very likely indicate pronounced local variations of the residual stress of the TiN film. Improved future analyses would therefore call for measurements and consideration of local stress fluctuations and effects of tapering of the fins along their height.[26]

In Figure 4, we also show the theoretical wavelength dependence of the buckling critical stress of a TiN beam by itself, with the moduli and dimensions taken to correspond to those of sample A. This is the known Euler's critical stress of a beam of length $\lambda/2$ at buckling, $\sigma_c^{\mathrm{beam}} = 4\pi^2 E_{\mathrm{beam}} I_{\mathrm{beam}}/(\lambda^2 A_{\mathrm{beam}})$.[28] As shown in Figure 4, the buckling states of the fins deviate from the Eulerian formula: although the buckling critical stress of a beam varies monotonically with the length, the buckling state of a beam-stiffened plate can be realized only above a minimum critical stress above which the work of the

DOI: 10.1021/acs.nanolett.5b00685
Nano Lett. 2015, 15, 3845−3850

compressive stress from the beam offsets the bending energies of the beam and plate. Moreover, at a given critical stress above the minimum critical stress, the beam-stiffened plate can accommodate wavelengths within the range defined by that stress value around the minimum. This correlation is well fulfilled for samples A and B, but it is less accomplished in the case of sample C, for which a shift to shorter wavelengths is observed. This is because the stress in sample C is very close to the minimum critical stress for that sample. Small wavelengths also suggest possible nonuniformities of the stress and geometry along the beam; such local variations in stress and dimensions diminish the long-range periodicity and favor correlated buckling over shorter lengths (Figure 4). This is also consistent with the observation of incipient, uncorrelated buckling in sample D at stresses below the theoretical minimum critical buckling stress.

We have analyzed the minimum critical buckling stress of TiN-capped fins as a function of TiN and ILD dimensions over relevant ranges. From eq 1, we have found that for a given height of the TiN cap, the fins remain unbuckled at higher stresses as they are wider and have shorter ILD ridges. Alternatively, for a given height of the ILD ridges, the fins can remain stable at smaller heights and larger widths of TiN caps. These results are in good agreement with those derived from finite element mechanical analysis of the bifurcation buckling of similar TiN-capped ILD fins.[25,26,33]

Figure 5a shows the trade-off between the height of the TiN cap and that of the ILD ridge for a given width (d = 32 nm) for samples C and D. These samples can sustain higher stresses for either (i) shorter TiN caps for a given ILD height or (ii) shorter ILD ridges for a given TiN height. In each case, a reduction of the total bending energy is accomplished by reducing the total height of the fin, although a more efficient control is provided by adjusting the height of the cap (i.e., the thickness of the TiN mask). For example, from Figure 5a, we note that in order to remain unbuckled under stresses around 1.5 GPa, the 32 nm wide fins should be made either of a 200 nm tall ILD and a 12 nm thick TiN cap or a 400 nm tall ILD and a 4 nm thick TiN cap. Although the residual stress of the TiN caps is the same (1.4 GPa) for both samples C and D, the shorter ILD ridge of sample D prevents its buckling. As shown in Figure 5a, the theoretically predicted 1.5 GPa border between buckled (sample C) and unbuckled (sample D) states of the two samples agrees very well with the measurements shown in Figure 4. The dependence of the minimum critical buckling stress on all three dimensions (ILD height h_{ILD}, cap height h_{TiN}, fin width d) is shown in Figure 5b in the form of isosurfaces at 0.5 and 2.0 GPa. Such minimum critical stress isosurfaces in the (d, h_{ILD}, h_{TiN}) space provide the general solution for stable configurations that can remain unbuckled for a given residual stress of the TiN mask.

In conclusion, we have analyzed the nanoscale buckling of patterned TiN-capped ILD fins by intertwining measurements and calculations. The wavelength dependence of the critical buckling stress has been calculated from the buckling equation, the experimental points on these curves have been obtained from dimensional measurements, the buckling states have been determined from topography measurements, and the buckling/unbuckling stress curves have been compared with residual stress values from wafer curvature measurements. Our combined experimental and theoretical analysis offers working points (dimensions and mechanical properties) for buckling-free structures, and the proposed analytical model for the buckling stress provides a framework for guiding the design of future nanoscale interconnect architectures.

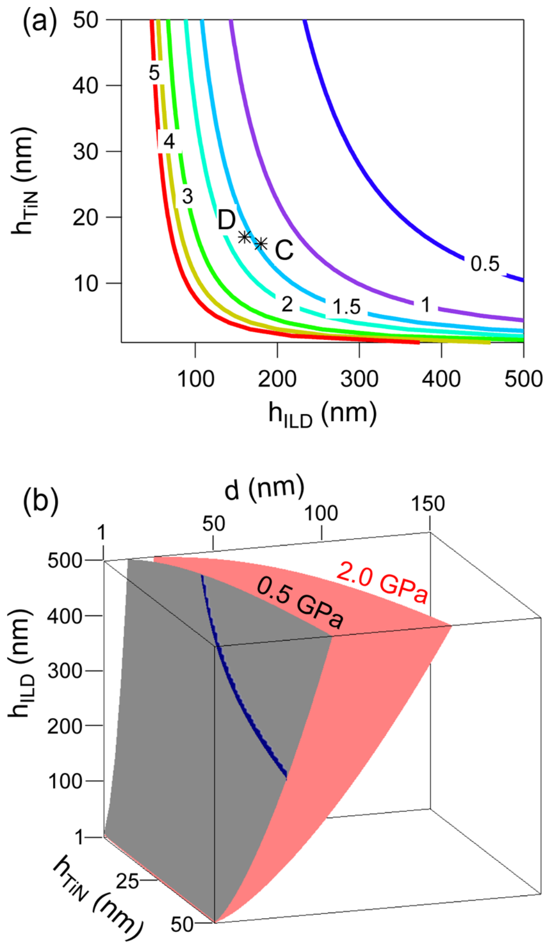

Figure 5. (a) Contours of the minimum critical buckling stress from 0.5 to 5.0 GPa in the (h_{ILD}, h_{TiN}) plane (fin width 32 nm). Each contour is labeled with the critical stress value in GPa, and separates the unbuckled (left) from buckled (right) states of fins of various dimensions. (b) Critical stress isosurfaces at σ_c = 0.5 GPa and σ_c = 2.0 GPa in the (d, h_{ILD}, h_{TiN}) space. Each isosurface separates the buckled (left and front) from the unbuckled (right and behind) states of fins of various dimensions. The blue contour highlights the intersection between the 0.5 GPa isosurface and the (h_{ILD}, h_{TiN}) plane at d = 32 nm; the same blue contour is labeled 0.5 GPa in panel a. The stack structure and material parameters correspond to samples C and D.

Methods. *General.* Certain commercial equipment, instruments, or materials are identified in this document. Such identification does not imply recommendation or endorsement by the National Institute of Standards and Technology, nor does it imply that the products identified are necessarily the best available for the purpose.

Sample Fabrication. The ILD film stack consists of 100 nm SiO_2 deposited by chemical vapor deposition (CVD) directly on the Si wafer, followed by a 12 nm dense (k = 4.80) SiOC:H etch stop film deposited by plasma enhanced CVD (PECVD).[34] Low-k dielectric a-C:H (k = 2.25) (samples A and B) and a-SiOC:H (k = 2.65) (samples C and D) ILD films (about 200 nm thick) were deposited on the SiO_2/SiOC:H film stack by spin-on deposition and PECVD, respectively.[35,36] The SiO_2/SiOC:H/ILD dielectric film stack was capped with a 40 nm (for samples A and B) to 20 nm (for samples C and D)

DOI: 10.1021/acs.nanolett.5b00685
Nano Lett. 2015, 15, 3845−3850

thick TiN hardmask deposited by standard physical vapor deposition methods.

Nanoscale trenches were formed in the ILD via standard lithographic, spacer based pitch division, and plasma etching procedures.[37] Briefly, standard 193 nm immersion lithography was utilized to pattern photoresist structures with a minimum 160 nm pitch. A spacer material was then deposited over the photoresist and the photoresist was subsequently selectively removed to produce a minimum 80 nm pitch grating in the spacer material with 40 nm wide lines and spaces. A standard TiN plasma etch process was then utilized to selectively transfer the resulting spacer pattern into the TiN mask. The spacer pattern was then selectively removed utilizing standard wet chemical and ash procedures. The 80 nm grating pattern formed in the TiN mask was finally transferred into the ILD using a second plasma etch, optimized for the particular ILD material of interest.

■ ASSOCIATED CONTENT

Ⓢ Supporting Information

A brief description of elastic moduli measurements using CR-AFM and the full derivation of the buckling analysis for a beam-stiffened plate are provided in support of the results presented above. The Supporting Information is available free of charge on the ACS Publications website at DOI: 10.1021/acs.nanolett.5b00685.

■ AUTHOR INFORMATION

Corresponding Authors

*E-mail: gheorghe.stan@nist.gov

*E-mail: cciobanu@mines.edu.

Notes

The authors declare no competing financial interest.

■ REFERENCES

(1) Meindl, J. D.; Chen, Q.; Davis, J. A. *Science* **2001**, *293*, 2044–2049.
(2) Lundstrom, M. *Science* **2003**, *299*, 210–211.
(3) Lieber, C. M. *MRS Bull.* **2003**, *28*, 486–491.
(4) Vogel, E. M. *Nat. Nanotechnol.* **2007**, *2*, 25–32.
(5) King, S. W.; Simka, H.; Herr, D.; Akinaga, H.; Garner, M. *APL Mater.* **2013**, *1*, 040701.
(6) Rogers, J. A.; Someya, T.; Huang, Y. *Science* **2010**, *327*, 1603–1607.
(7) Stan, G.; Ciobanu, C. V.; Parthangal, P. M.; Cook, R. F. *Nano Lett.* **2007**, *7*, 3691–3697.
(8) Stan, G.; Ciobanu, C. V.; Thayer, T. P.; Wang, G. T.; Creighton, J. R.; Purushotham, K. P.; Bendersky, L. A.; Cook, R. F. *Nanotechnology* **2009**, *20*, 035706.
(9) Stan, G.; King, S. W.; Cook, R. F. *Nanotechnology* **2012**, *23*, 215703.
(10) Lomonosov, A. M.; Ayouch, A.; Ruello, P.; Vaudel, G.; Baklanov, M. R.; Verdonck, P.; Zhao, L.; Gusev, V. E. *ACS Nano* **2012**, *6*, 1410–1415.
(11) Treacy, M. M. J.; Ebbesen, T. W.; Gibson, J. M. *Nature* **1996**, *381*, 678–680.
(12) Uchic, M. D.; Dimiduk, D. M.; Florando, J. N.; Nix, W. D. *Science* **2004**, *305*, 986–989.
(13) Jang, D.; Greer, J. R. *Nat. Mater.* **2010**, *9*, 215–219.
(14) Baklanov, M. R.; de Marneffe, J.-F.; Shamiryan, D.; Urbanowicz, A. M.; Shi, H.; Rakhimova, T. V.; Huang, H.; Ho, P. S. *J. Appl. Phys.* **2013**, *113*, 041101.
(15) Stan, G.; Gates, R. S.; Kavuri, P.; Torres, J.; Michalak, D.; Ege, C.; Bielefeld, J.; King, S. W. *Appl. Phys. Lett.* **2014**, *105*, 152906.
(16) Edelstein, D.; Heidenreich, J.; Goldblatt, R.; Cote, W.; Uzoh, C.; Lustig, N.; Roper, P.; McDevitt, T.; Motsiff, W.; Simon, A.; Dukovic, J.; Wachnik, R.; Rathore, H.; Schulz, R.; Su, L.; Luce, S.; Slattery, J. Full copper wiring in a sub-0.25 μm CMOS ULSI technology. *IEEE Int. Electron Devices Meet.* **1997**, 773–776.
(17) Maex, K.; Baklanov, M. R.; Shamiryan, D.; Iacopi, F.; Brongersma, S. H.; Yanovitskaya, Z. S. *J. Appl. Phys.* **2003**, *93*, 8793–8841.
(18) Fayolle, M.; Passemard, G.; Louveau, O.; Fusalba, F.; Cluzel, J. *Microelectron. Eng.* **2003**, *70*, 255–266.
(19) Bowden, N.; Brittain, S.; Evans, A. G.; Hutchinson, J. W.; Whitesides, G. M. *Nature* **1998**, *393*, 146–149.
(20) Chen, X.; Hutchinson, J. W. *J. Appl. Mech.* **2004**, *71*, 597–603.
(21) Huang, R. *J. Mech. Phys. Solids* **2005**, *53*, 63–89.
(22) Stafford, C. M.; Harrison, C.; Beers, K. L.; Karim, A.; Amis, E. J.; Vanlandingham, M. R.; Kim, H. C.; Volksen, W.; Miller, R. D.; Simonyi, E. E. *Nat. Mater.* **2004**, *3*, 545–550.
(23) Khang, D. Y.; Jiang, H. Q.; Huang, Y.; Rogers, J. A. *Science* **2006**, *311*, 208–212.
(24) Jiang, H.; Khang, D.-Y.; Song, J.; Sun, Y.; Huang, Y.; Rogers, J. A. *Proc. Natl. Acad. Sci. U.S.A.* **2007**, *104*, 15607–15612.
(25) Darnon, M.; Chevolleau, T.; Joubert, O.; Maitrejean, S.; Barbe, J. C.; Torres, J. *Appl. Phys. Lett.* **2007**, *91*, 194103.
(26) Ducote, J.; Posseme, N.; David, T.; Darnon, M.; Chevolleau, T.; Guillermet, M. *Appl. Phys. Lett.* **2014**, *104*, 231603.
(27) Miles, A. J. *J. Appl. Mech.* **1936**, *3*, A-47.
(28) Timoshenko, S.; Gere, J. *Theory of elastic stability*, 2nd ed.; McGraw-Hill: New York/London, 1961; Ch. 8, 9.
(29) Huang, Z. Y.; Hong, W.; Suo, Z. *J. Mech. Phys. Solids* **2005**, *53*, 2101–2118.
(30) Cendula, P.; Kiravittaya, S.; Mei, Y. F.; Deneke, C.; Schmidt, O. G. *Phys. Rev. B* **2009**, *79*, 085429.
(31) Tirumala, V. R.; Stafford, C. M.; Ocola, L. E.; Douglas, J. F.; Mahadevan, L. *Nano Lett.* **2012**, *12*, 1516–1521.
(32) Mora, T.; Boudaoud, A. *Eur. Phys. J. E: Soft Matter Biol. Phys.* **2006**, *20*, 119–124.
(33) Posseme, N.; David, T.; Chevolleau, T.; Darnon, M.; Brun, P.; Guillermet, M.; Oddou, J. P.; Barnola, S.; Bailly, F.; Bouyssou, R.; Ducote, J.; Hurand, R.; Verove, C.; Joubert, O.; Wu, H.; Claeys, C.; Kuo, Y.; Lai, K.; Philipossian, A.; Jiang, T.; Xiaoping, S.; Lin, Q.; Huang, D.; Huang, R.; Zhang, Y.; Liu, R.; Song, P. Porous SiOCH integration: Etch challenges with a trench first metal hard mask approach. *ECS Trans.* **2011**, 389–394.
(34) King, S. W.; French, M.; Jaehnig, M.; Kuhn, M.; French, B. *Appl. Phys. Lett.* **2011**, *99*, 202903.
(35) Zhou, W.; Bailey, S.; Sooryakumar, R.; King, S.; Xu, G.; Mays, E.; Ege, C.; Bielefeld, J. *J. Appl. Phys.* **2011**, *110*, 043520.
(36) Bailey, S.; Mays, E.; Michalak, D. J.; Chebiam, R.; King, S.; Sooryakumar, R. *J. Phys. D: Appl. Phys.* **2013**, *46*, 045308.
(37) van Veenhuizen, M.; Allen, G.; Harmes, M.; Indukuri, T.; Jezewski, C.; Krist, B.; Lang, H.; Myers, A.; Schenker, R.; Singh, K. J.; Turkot, R.; Yoo, H. J. Demonstration of an electrically functional 34 nm metal pitch interconnect in ultralow-k ILD using spacer-based pitch quartering. *IEEE Int. Interconnect Technol. Conf., Proc.* **2012**, 1–3 DOI: 10.1109/IITC.2012.6251665.

DOI: 10.1021/acs.nanolett.5b00685
Nano Lett. 2015, 15, 3845–3850